Chapter 8

Precipitation behaviour of NF709 and NF709R under static ageing at 750 °C and 800 °C

8.1 Introduction

NF709, a 20Cr-25Ni austenitic steel, manufactured by Nippon Steel, is currently set as a standard for its creep and corrosion resistance. Studying its microstructural evolution during ageing at elevated temperatures is of great interest, both to ensure that no phase forms which is detrimental to creep properties and which could invalidate the extrapolations of short-term creep tests, and to identify a precipitation sequence which cannot be deduced from the existing literature. NF709 has a composition which distinguishes it from the existing 20/25, as it contains a unique combination of carbon and nitrogen together with niobium and titanium.

8.2 Material and experimental procedures

Two grades of NF709 were provided by National Power. The compositions are given in table 8.1. Little information could be obtained about the production route and the exact heat treatment: NF709R was cold-drawn, solution treated at 1200 °C and water quenched; the duration of the solution treatment is unknown. The solution-treatment temperature for NF709 is also unknown but is stated to be above 1100 °C. The experimental methods

NF709	Cr	Ni	Mn	Mo	Si	Nb	Ti	N	C	B	P
wt%	20.28	24.95	1.00	1.50	0.41	0.26	0.05	0.167	0.06	0.005	0.006
NF709R	Cr	Ni	Mn	Mo	Si	Nb	Ti	N	C	B	P
wt%	22.22	25.34	0.92	1.40	0.38	0.24	0.05	0.17	0.03	0.005	0.022

Table 8.1: Compositions of the two grades of NF709 provided by National Power. In both cases, S is 0.001 wt%

mentioned below are described in greater detail in chapter 7.

Samples were sealed in argon and aged in furnaces at 750 and 800 °C. Specimens for optical microscopy were electrolytically etched with a solution of 10% (by mass) oxalic acid in distilled water for general etching, and in a solution of 56 g / 100 ml KOH in distilled water for outlining σ-phase, according to the procedures described in [8].

Thin foils for TEM (transmission electron microscopy) examination were electropolished using a solution of 5% perchloric acid in 2n-ethoxy-butanol, in a twin-jet electropolisher.

Extraction was performed by dissolving the matrix electrolytically with a solution of 10% HCl in methanol at 5-6 V. The residues were then filtered with a membrane filter of 0.2 μm pore size. It was verified by prolonged centrifugation that no detectable amount of particles were left in the solution after filtration. X-ray analysis was performed in a 2-θ diffractometer.

8.3 As-received material

8.3.a Prediction of the phases present in the as-received state

It is difficult to make meaningful predictions for the as-received state as the exact conditions of solution treatment are not known. Table 8.2 shows the predicted phases and their amounts at the given solution treatment temperatures, 1100 °C for NF709 and 1200 °C for NF709R.

Since both tubes underwent different solution treatments and probably different mechanical treatments, it was necessary to characterise the as-received condition thoroughly. The two materials had substantially different initial hardnesses and grain sizes (table 8.3).

	NbN wt%	TiN wt%
NF709	0.260	0.064
NF709R	0.200	0.063

Table 8.2: Predicted equilibrium precipitates and their weight fractions at the solution treatment temperatures for each steel.

	HV 10 kg	Average grain size
NF709	178 ± 1.0	51 μm
NF709R	162 ± 1.6	90 μm

Table 8.3: Initial hardnesses and grain sizes of NF709 and NF709R. Grain sizes calculated according to [106].

The X-ray analysis of extraction residues showed further differences between the two steels. As indicated in table 8.4, NF709 does not seem to contain any Z-phase in the as-received state but instead contains substantial amounts of NbN. By contrast, NF709R does not show NbN but traces of Z-phase.

	NbC (38-1364)	NbN (38-1155)	TiC (32-1383)	(Nb,Ti)C (47-1418)	TiN (38-1420)	CrNbN (25-0591)
NF709		VS		VS	VS	
NF709R					S	VW

Table 8.4: Results of X-ray analysis of extraction residues for the two as-received materials (VS: very strong, S: strong, W: weak, VW: very weak).

These results are in agreement with SEM (scanning electron microscopy) observations. Relatively large precipitates are found in both steels (up to 3 μm for TiN and 1 μm for NbX). Their sizes are typical of residual precipitates, which are not dissolved during the solution treatment. But, while TiN is found in both steels, the EDX (energy dispersive X-ray) spectra of Nb rich particles revealed the presence of a substantial amount of Cr, giving a composition closer to that expected for Z-phase.

Because it was not clear whether this difference should be attributed to a different solution treatment or to the difference in chemical composition, samples of both steels were solution treated 2 h at 1200 °C. Both steels reacted fairly differently, with NF709 showing exaggerated grain growth and presenting a bimodal grain size distribution, while NF709R still presented a normal grain size distribution (see figure 8.2). In both cases, the weight fraction of filtered residues was smaller than in the as-received state. X-ray

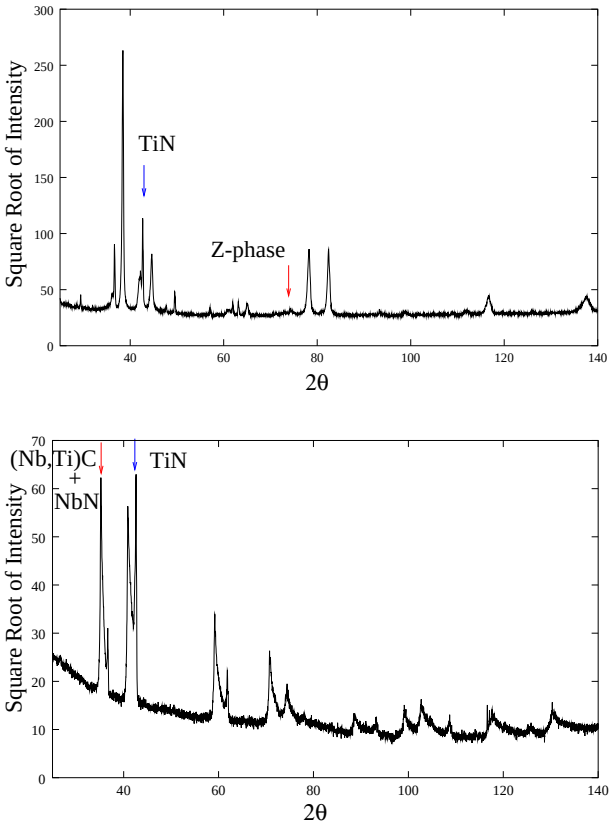

Figure 8.1: X-Ray diffraction on extraction residues for as received NF709R, the main peaks for identified phases are given, other peaks are all related to one of the two phases or the Al support

analysis did not reveal any change in the nature of the phases present (see table 8.4), which were the same as for the as-received samples. The new grain sizes are given in table 8.5.

	HV 10 kg	Average grain size
NF709	157 ± 2	$146 \pm 30\mu$m
NF709R	158 ± 2	$128 \pm 10\mu$m

Table 8.5: Hardness and grain size of NF709 and NF709R after 2 h at 1200 °C. Grain size calculated according to [106].

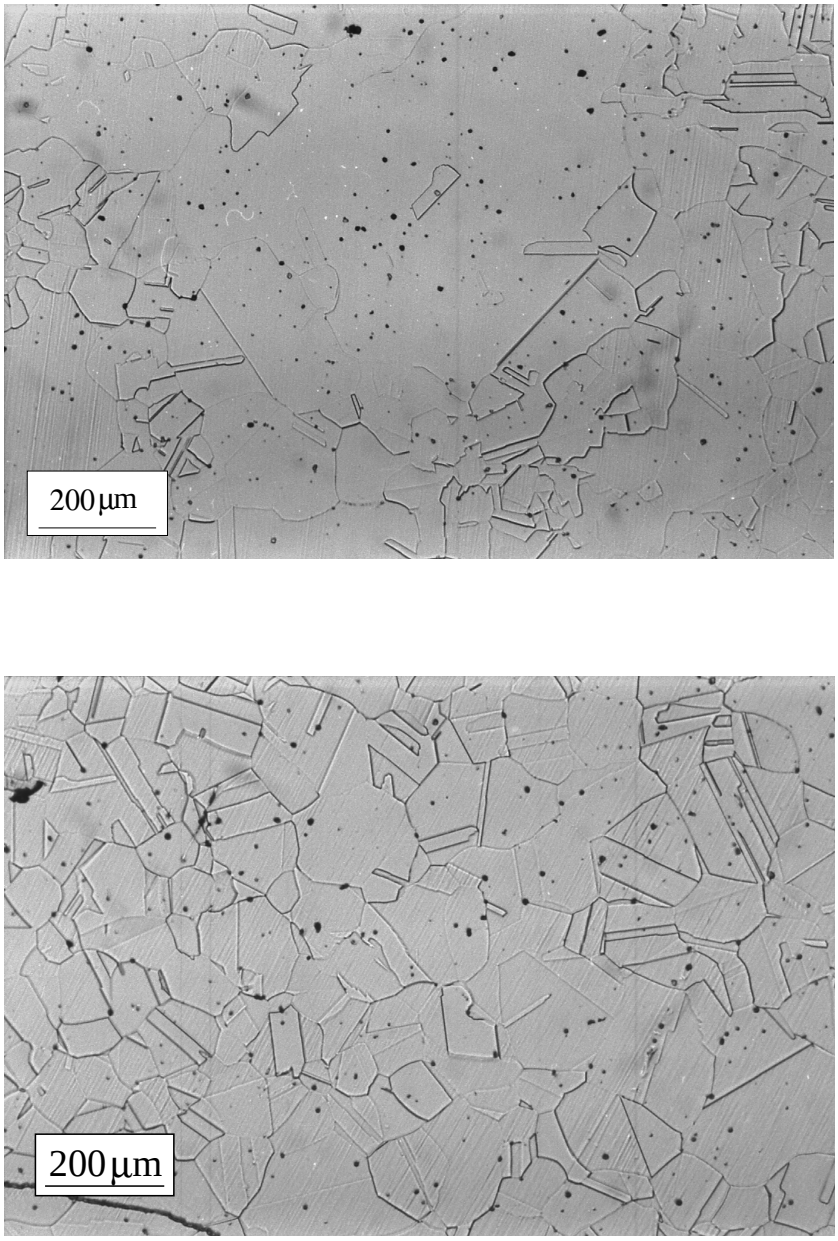

Figure 8.2: Microstructure of NF709 and NF709R after 2 h at 1200 °C. Etched 60 s in a 10 wt% solution of oxalic acid in water.

8.4 Short term ageing

Specimen of NF709 and NF709R were aged for 1 h, 100 h (NF709) and 200 h at 750°C. Extraction results (figure 8.3) show that the precipitation of $M_{23}C_6$ occurs at very early stages, although subsequent changes in the X-ray spectra of the residues indicate it is not yet completed.

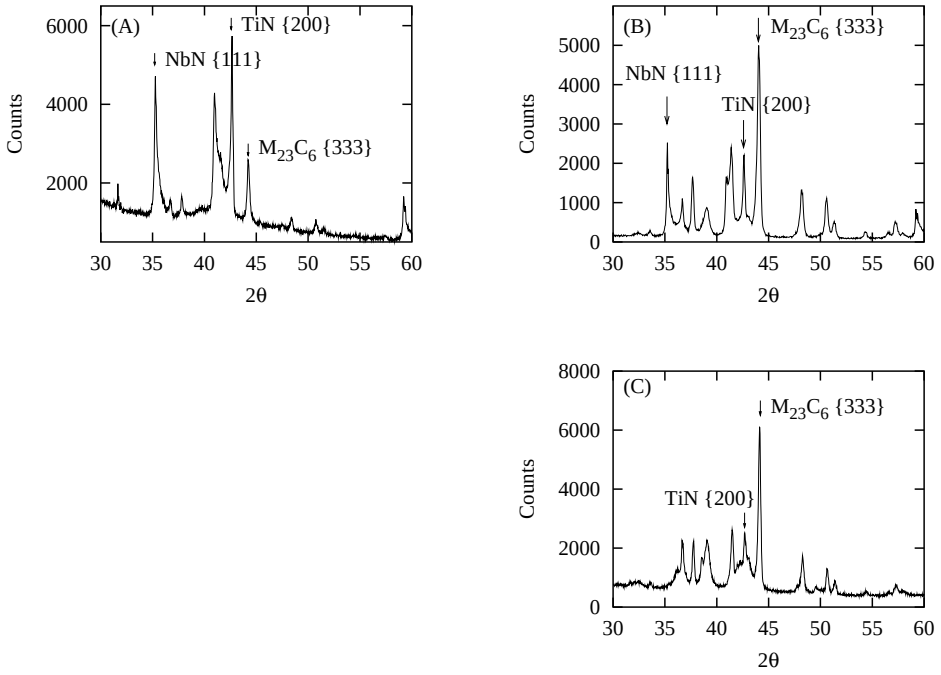

Figure 8.3: X-ray analysis of extracted residues for NF709 aged 1 h (A) and 200 h (B) at 750 °C, and NF709R aged 200 h (C) at 750 °C. Only the most intense peak for each phase is indicated, all other peaks have been identified as belonging to the identified phases, but are not indexed for clarity.

The morphology and distribution of the precipitates differs significantly between the two variants of NF709. Figure 8.4 shows optical micrographs of NF709 and NF709R aged 200 h at 750 °C. The alignment of precipitates observed in the 22Cr variant is not found in the 20Cr sample. Both steels show relatively intense precipitation on grain boundaries, incoherent twin boundaries, and, to a lesser extent, on coherent twin boundaries.

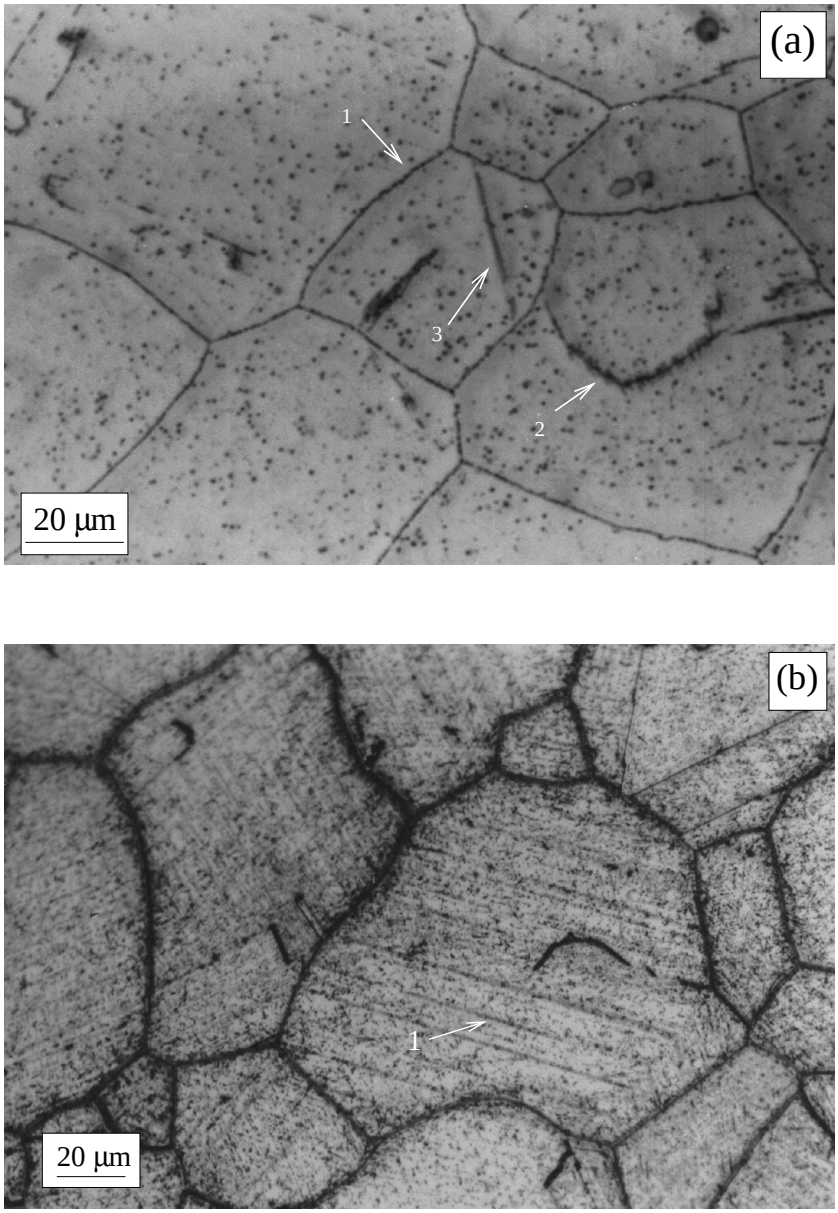

Figure 8.4: NF709 (a) and NF709R (b) after 200 h at 750 °C, etched 10 s in a 10 wt% solution of oxalic acid in water. (a/1) points to grain boundary precipitates, (a/2) to incoherent twin boundary precipitates and (a/3) to coherent twin boundary precipitates. (b/1) shows alignment of precipitates.

8.4.a TEM identification of the phases present in NF709

In addition to the phases identified by X-ray analysis of extracted residues, TEM investigation of carbon replicas revealed the formation of Z-phase (CrNbN) on dislocations, as shown in figure 8.5.

$M_{23}C_6$ was found at numerous sites, as shown in figure 8.6: strong presence on grain boundaries, with a globular morphology, on incoherent and coherent twin boundaries with a plate morphology, and around residual NbX residual precipitates. All these occurrences are well documented and have been reported on numerous occasions, with the exception of the formation of plates around residual NbX particles which is more seldom reported (chapter 2). As reported in the literature, $M_{23}C_6$ has a cube-to-cube orientation relationship with the austenite, and its lattice parameter is three times that of the matrix; typical diffraction patterns appear as shown in figure 8.6 (d) and (f). After identification by diffraction and EDX, it became evident that EDX fingerprints were sufficient to distinguish $M_{23}C_6$ and Z-phase without possible confusion.

It is interesting to note the differences between the results obtained by X-ray analysis of extracted residues, and those obtained using TEM, particularly with regard to Z-phase. Although this phase is found with the latter, it was not detected with the former method. One of the possible causes is the size of the Z-phase precipitates. As can be seen in figure 8.5, these are seldom more than 50 nm in length after 200 h of heat treatment at 750 °C. This is significantly smaller than the 200 nm pore size of the membrane filter. To verify whether Z-phase particles were retained by the filter, the filtered solution was centrifuged. Since no deposit was found after prolonged centrifuging, it can be concluded that Z-phase was either dissolved or its quantity was too small to give a significant signal. Z-phase is found, with this method, in the as-received NF709R because it is present as residual particles, that is, coarse particles formed during solidification and undissolved by the solution treatment. By contrast, Z-phase formed during ageing was never found in the extracted residues.

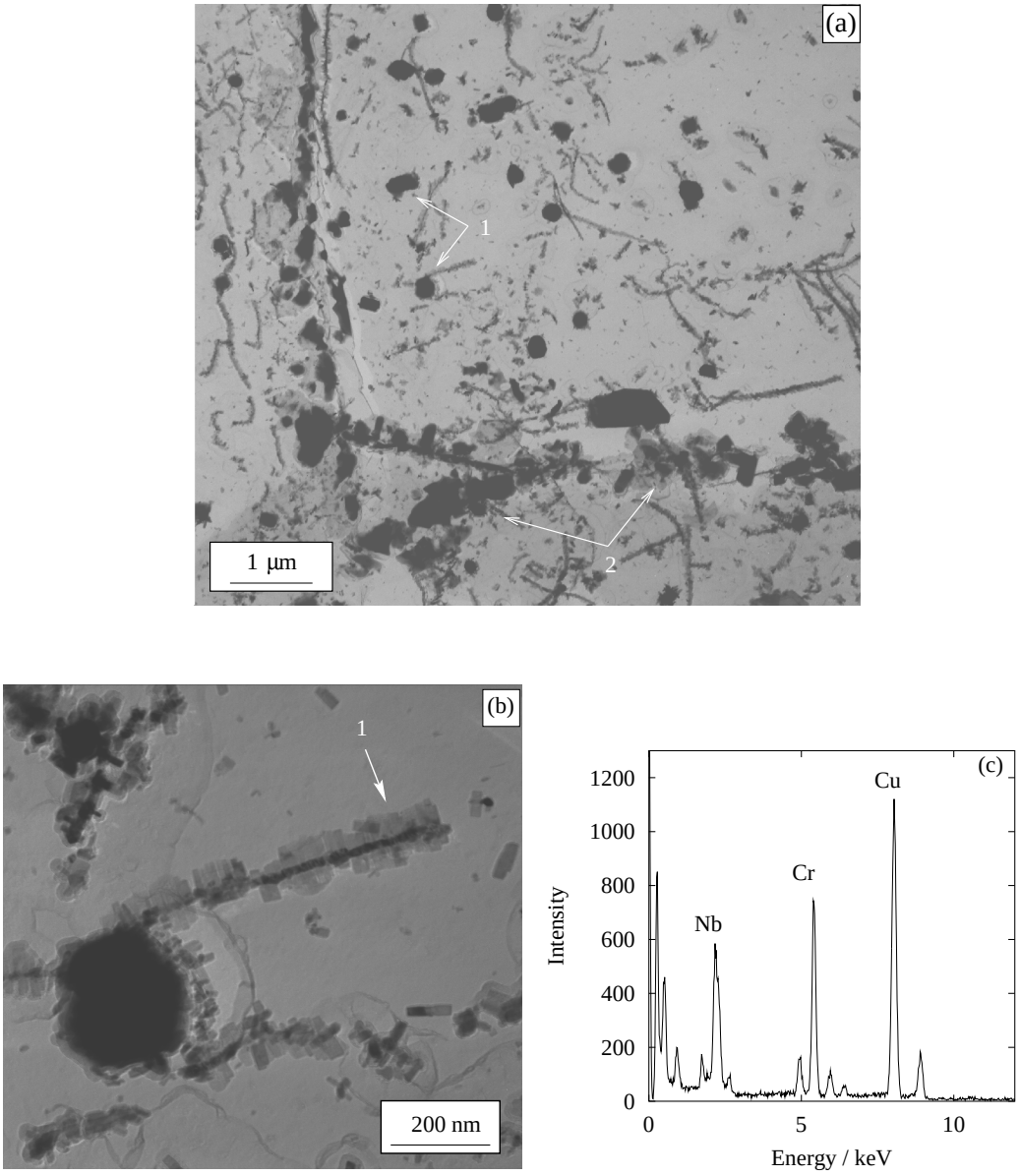

Figure 8.5: Transmission electron micrographs of a carbon replica of NF709 after 200 h at 750 °C, (a) low magnification image, with $M_{23}C_6$ on (a/1) residual NbN and on (a/2) grain boundaries; (b) high magnification image showing (b/1) Z-phase precipitates on a dislocation, and (c) EDX spectrum from the particles identified by the arrow in (b), the strong copper signal comes from the grid supporting the replica.

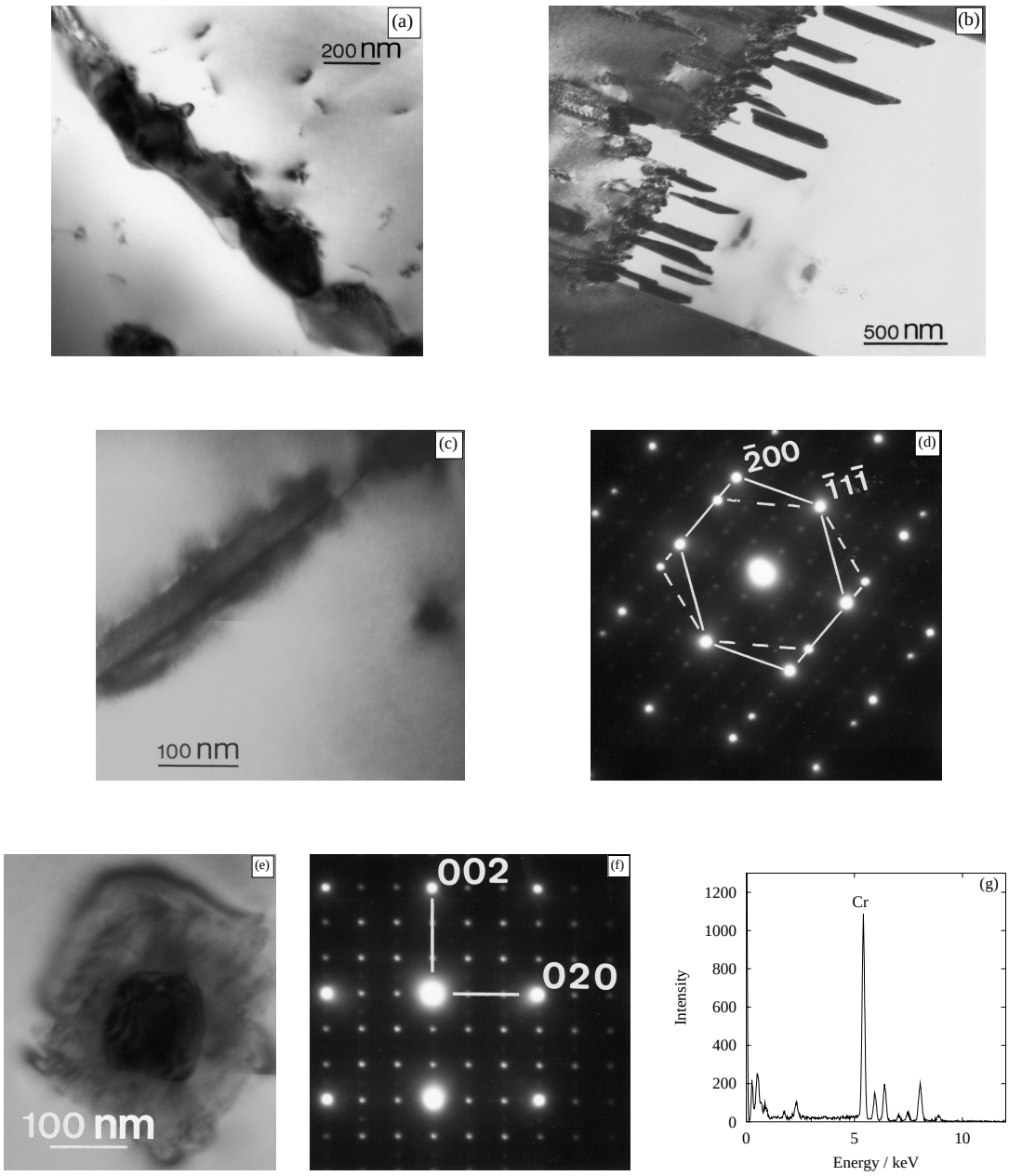

Figure 8.6: The various locations and morphologies of $M_{23}C_6$ in NF709 after 100 h at 750 °C: (a) forming on grain boundaries, (b) as plates on incoherent twin boundaries, and (c) on coherent twin boundaries (less frequent). (d) Diffraction pattern from the precipitate shown in (c), the indexed points are for austenite and show the two orientations on each side of the twin boundary; $M_{23}C_6$ has a lattice parameter about three times larger than that of austenite, but has the same structure and a cube-to-cube orientation relationship. (e) Plate forming around a NbX residual particle (formed during solidification and undissolved by the solution treatment), (f) typical diffraction pattern from $M_{23}C_6$ with the austenite points indexed, and (g) typical EDX spectrum.

8.4.b $M_{23}C_6$ after very short ageing

The precipitation of $M_{23}C_6$ is well advanced after 200 h at 750 °C. Both optical microscopy and TEM reveal continuous arrays of relatively coarse precipitates on the grain boundaries. Very short term aging was performed at 750 °C to estimate the speed of transformation and to verify whether the predicted composition shift was observed (chapter 6).

Figure 8.7 shows $M_{23}C_6$ precipitates on grain boundaries in NF709, after 1 h at 750 °C. The composition, after correction to include the expected mass fraction of carbon (which is not measured by EDX) is presented in table 8.6. The Fe content is significantly larger than the equilibrium value.

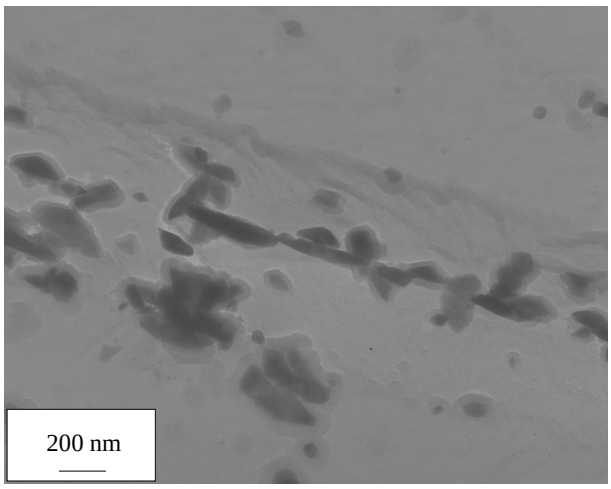

Figure 8.7: Transmission electron micrograph of a carbon replica of NF709 after 1 h at 750 °C, showing $M_{23}C_6$ formed on grain boundaries.

Element	Cr	Fe	Ni	Mo
Wt%	55.0	16.8	3.2	10.8

Table 8.6: The average composition of $M_{23}C_6$ after 1 h at 750°C.

8.4.c TEM identification of phases in NF709R

The same phases were identified in NF709R as in NF709. Figure 8.8 shows coarse $M_{23}C_6$ precipitates formed on the grain boundaries, in NF709R after 200 h at 750 °C.

However, the aligned precipitates visible in figure 8.4 were identified as Z-phase and are therefore present in quantities significantly greater than in NF709. Also, the aligned particles observed (figure 8.8 (a)), which clearly correspond to precise crystallographic planes, are not found in NF709. TEM investigation of thin foils of the as-received NF709R did not reveal an obvious difference in dislocation density, therefore making it difficult to explain the difference in the way the precipitation of Z-phase occurs in the two steels.

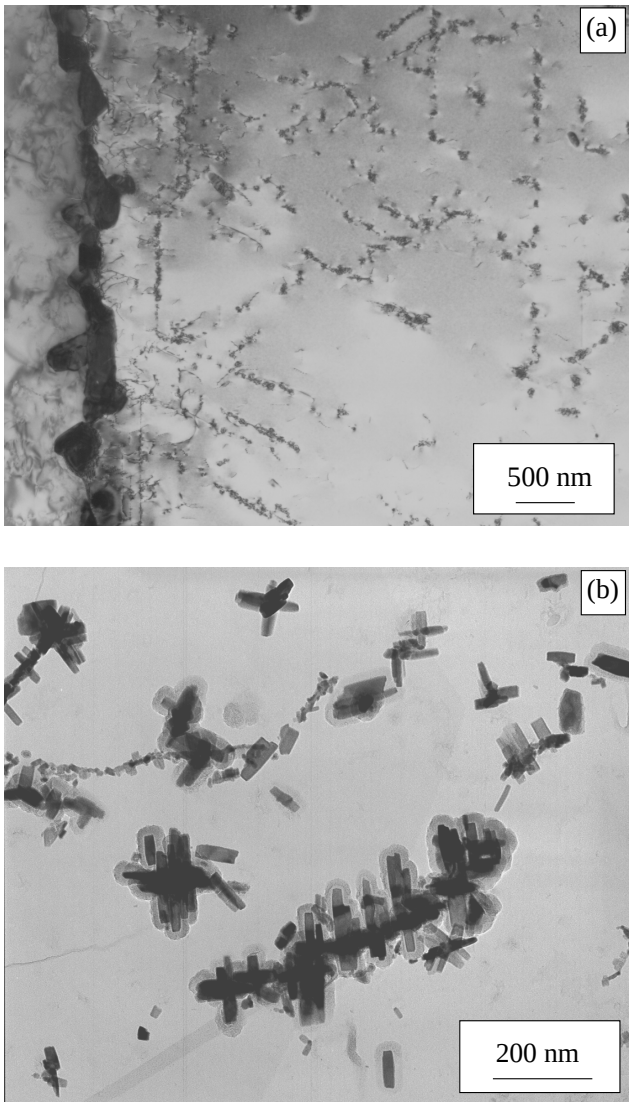

Figure 8.8: TEM micrographs (a) of a thin foil of NF709R after 200 h at 750 °C, showing a grain boundary decorated by $M_{23}C_6$ and alignment of Z-phase particles, (b) of a replica at higher magnification, showing Z-phase particles growing on a dislocation.

8.5 NF709 aged 2500 and 5000 h at 750 and 800 °C

Figure 8.9 shows optical micrographs of NF709 aged 2500 and 5000 h at both temperatures: both the grain and incoherent twin boundaries are covered with coarse precipitates, together with most of the coherent twin boundaries. Interesting results could be obtained

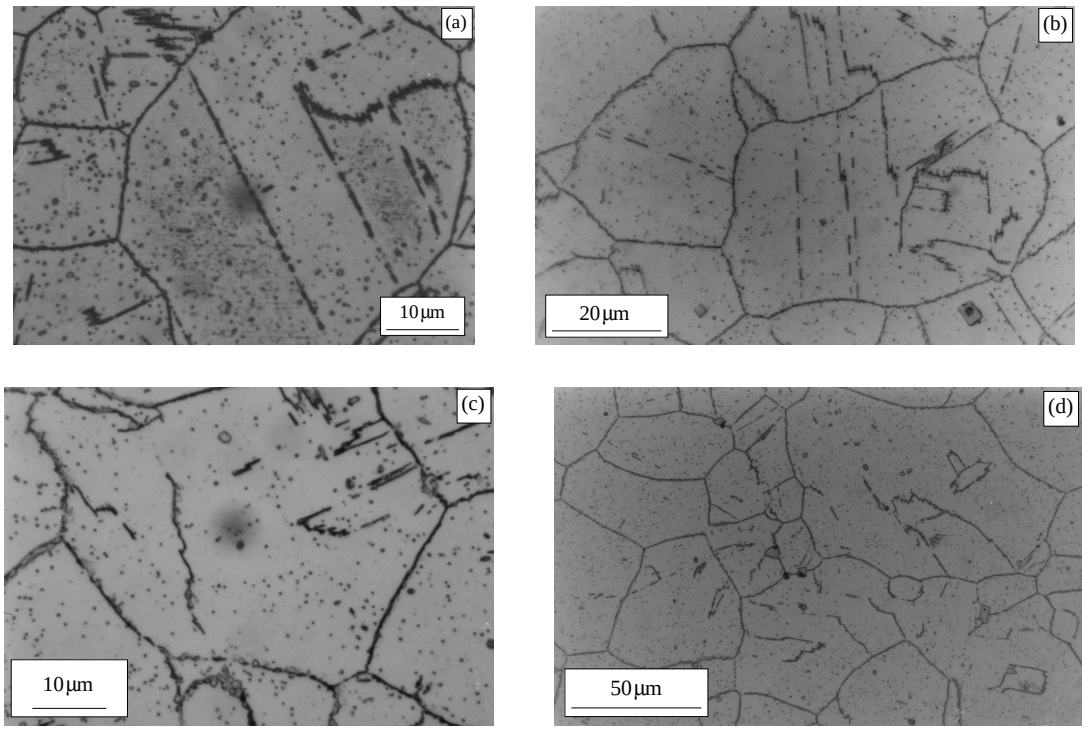

Figure 8.9: Optical micrographs of NF709 aged (a) 2500 h, (b) 5000 h at 750 °C, and (c) 2500 h, (d) 5000 h at 800 °C

from X-ray analysis of extracted residues: the relative intensity of the main peak for NbN is clearly reduced between the samples aged 2500 h and 5000 h at 800 °C, as illustrated in figure 8.10. This can be attributed to a dissolution of the residual NbN to the profit of Z-phase (CrNbN).

A careful examination of the X-ray spectra, for both 2500 h and 5000 h at 800 °C, also revealed a separation in the $M_{23}C_6$ peaks which was not detected by automated methods. As illustrated in figure 8.10 (c), this is true for specimen aged at 800 °C but not at 750 °C were only a small shoulder is visible near the top of the peak. Two distinct lattice parameters could be estimated corresponding to a cubic phase and a cubic diamond

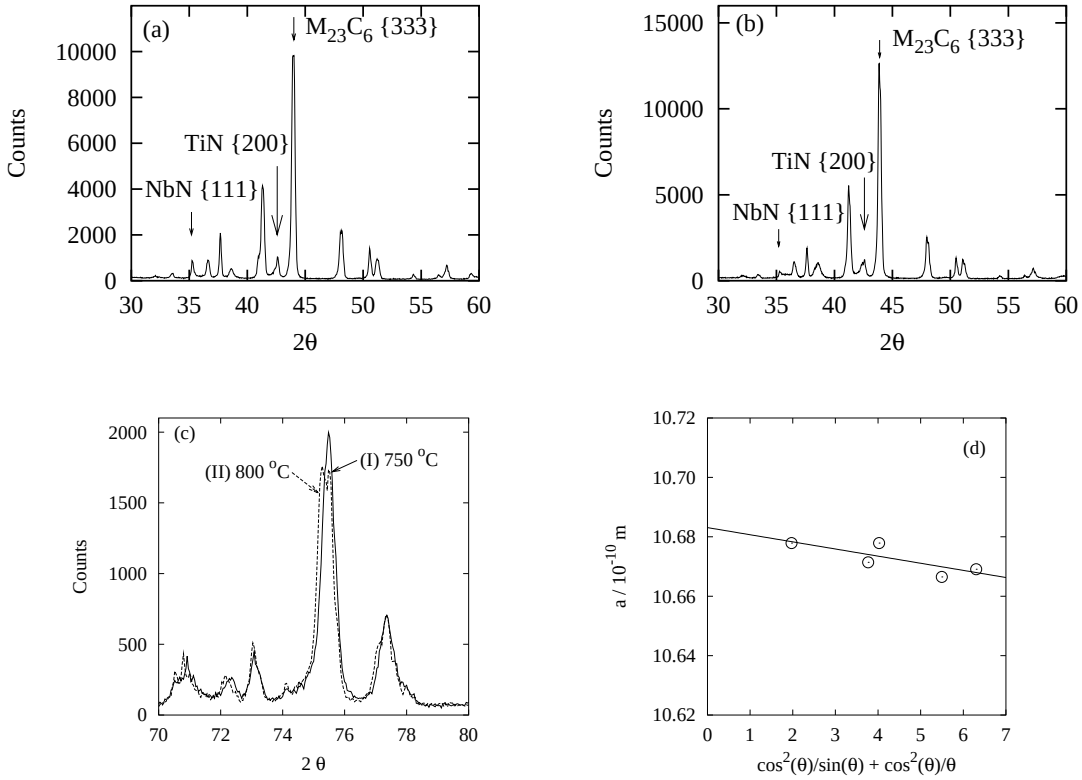

Figure 8.10: X-ray spectrum of extracted residues from NF709 aged (a) 2500 h and (b) 5000 h at 800 °C, and (c) comparison between the 2500 h at 750 °C and 800 °C showing a clear separation in the {660} peak of $M_{23}C_6$ at 800 °C; (d) accurate determination of the lattice parameter of $M_{23}C_6$ in NF709 after 2500 h at 800 °C, giving $a = 10.683$ Å

phase ($h + k + l$ all even with $h + k + l \neq 4n$ were absent so that the peaks for these indices were unique rather than showing the separation illustrated above). The measured lattice parameters are plotted as a function of $\cos^2(\theta)/\sin(\theta) + \cos^2(\theta)/\theta$, the Nelson-Riley function, and extrapolated to $\theta = 90°$ to minimise errors due to absorption [107]; this is illustrated in figure 8.10 (d). Table 8.7 presents the different lattice parameters measured for these ageing times. The lattice parameter measured for the diamond cubic phase, later identified as Cr_3Ni_2SiN is significantly greater than the one reported for Cr_3Ni_2SiC (10.62 Å, JCPDS 17-0330). Taking account of the literature covered in chapter 2, there is no previous record of the lattice parameter of Cr_3Ni_2SiN. The shoulder visible in figure 8.10 (c), for the peak (I) is evidence that the lattice parameter of this phase, formed at lower temperature, is significantly closer to that of $M_{23}C_6$. This might be related to the

composition change of Cr_3Ni_2SiX (where X refers to C or N): Williams [53] reported a significant increase in the Mo content of this phase with temperature (about 7 wt% per 100 °C), which could explain the significant change in the lattice parameter.

Phase / Ageing time	2500 h	5000 h
$M_{23}C_6$	10.683 Å	10.684 Å
Cr_3Ni_2SiN	10.713 Å	10.722 Å

Table 8.7: The lattice parameters of $M_{23}C_6$ and Cr_3Ni_2SiN at 800 °C for two different ageing times.

TEM examination of thin foils confirmed the presence of a new phase whose composition matches closely the reported compositions of Cr_3Ni_2SiX; diffraction confirmed a lattice parameter close to 10.7 Å, and the diamond-cubic structure for which particular extinction rules exist which have been mentioned earlier. This was, however, only seen in a few diffraction patterns; the presence of the unexpected diffraction spots (e.g. 200) in many others was attributed to double diffraction, as strong diffracted beams from the austenite may act as secondary diffraction sources.

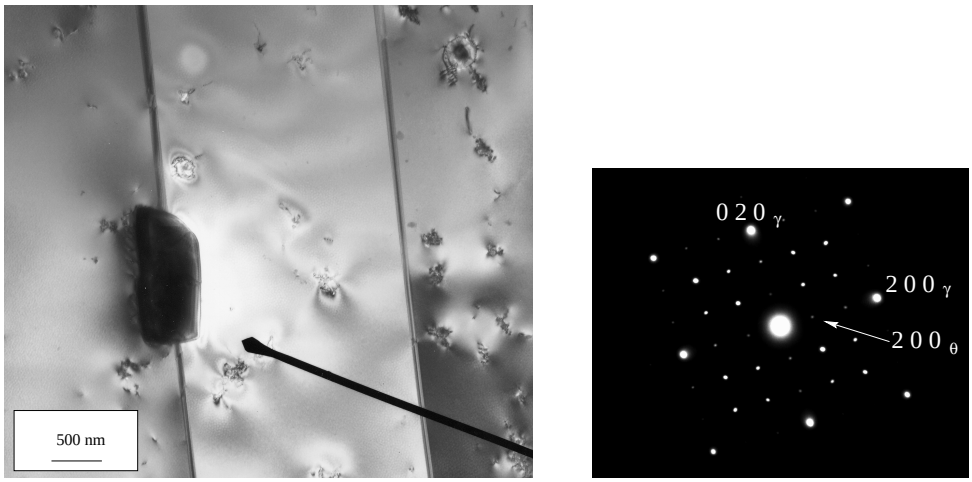

Figure 8.11: TEM micrographs of a thin foil of NF709 after 2500 h at 750 °C, showing a coarse Cr_3Ni_2SiN precipitate on a coherent twin boundary. Diffraction pattern of Cr_3Ni_2SiN precipitate, zone axis 001, indexed for austenite (γ) and Cr_3Ni_2SiN (θ), showing partial extinction of 200 from the precipitate (θ).

8.6 NF709R aged 2500 and 5000 h at 750 and 800 °C

As will be shown in this section, the precipitation sequence for the 22Cr version is fairly different from that of NF709, in spite of their relatively similar chemical compositions.

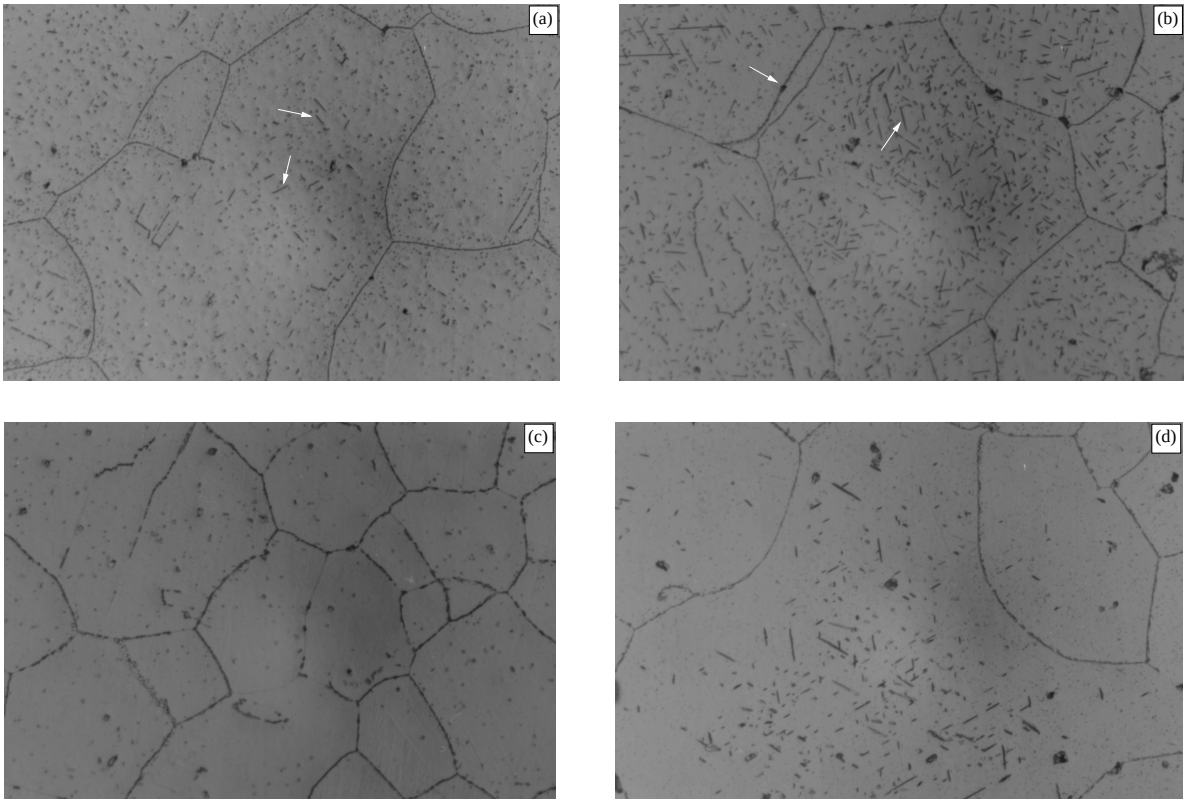

Figure 8.12: Optical micrographs of NF709R, aged (a) 2500 h and (b) 5000 h at 750 °C, and (c) 2500 and (d) 5000 h at 800 °C. The arrows point to σ-phase, which, after 2500 h at both temperatures or 5000 h at 800 °C is found only in the largest austenite grains.

After 2500 h at 750 °C, the microstructure reveals relatively dense intragranular precipitation. Precipitates of new morphologies are found on grain boundaries, similar to those shown in figure 8.12 (b), and within the grains, as pointed in figure 8.12 (a). The latter are found only in large grains. The same observations can be made after 5000 h at 800 °C, although to a lesser extent, as illustrated by figure 8.12 (c) where most of the smaller grains do not show new precipitates at the grain boundaries or new intragranular precipitates.

After 5000 h at 750 °C, the quantity of the coarse grain-boundary and, particularly,

of the plate-shaped precipitates has considerably increased, as shown by figure 8.12 (b); while at 800 °C, the plate-shaped intragranular particles are still essentially found in the larger grains.

Both these new particles were identified, using SEM, as σ-phase, of composition close to 44Cr 40Fe 10Ni 6Mo, at%, which is in satisfying agreement with the 46Cr 38Fe 10Ni 6Mo predicted with MTDATA for the same temperature.

The intragranular presence of σ-phase only in large grains is explained easily in terms of heterogenous nucleation: σ-phase nucleation is easier on sites such as triple points and grain boundaries. In grains of small sizes, the amount of surface for a given volume is more than in large grains, and there is therefore a greater number density of easy grain boundary nucleation sites for σ-phase. Because nucleation is more difficult within the grain, the tendency is for σ-phase to form intragranularly only if grain boundary sites are not available, and if the driving force for nucleation is large enough.

As is the case for NF709, a separation is observed between $M_{23}C_6$ and Cr_3Ni_2SiN, in the X-ray diffraction spectra of extracted residues, for NF709R, after 5000 h at 800 °C but not at 750 °C. As shown in figure 8.13, the separation is not as well defined as in NF709, and accurate lattice parameters could not be determined. However, two peaks are clearly overlapping, the one corresponding to the smaller lattice parameter this time having an intensity of only 50% of the other. This can be explained by the composition modifications presented by NF709R: the elements likely to control the amount of Cr_3Ni_2SiN such as Si or N are present in similar quantities, while the amount of C is halved, and as a consequence, the amount of $M_{23}C_6$ is reduced.

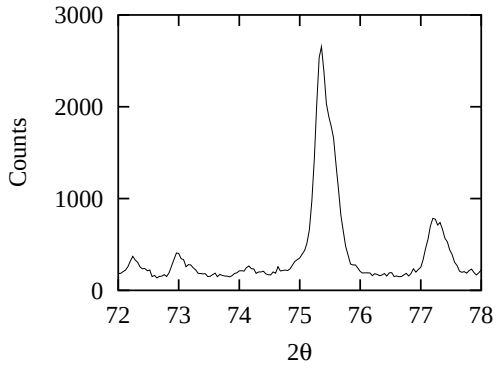

Figure 8.13: The {660} peak for $M_{23}C_6$ and Cr_3Ni_2SiN in NF709R after 5000 h at 800 °C, showing less separation than in NF709, shown in figure 8.10(c).

Electron diffraction and EDX in TEM confirmed the presence of σ-phase, as illustrated in figure 8.14 (c), while replicas revealed the presence of aligned Z-phase precipitates as observed after 200 h, figure 8.14 (a).

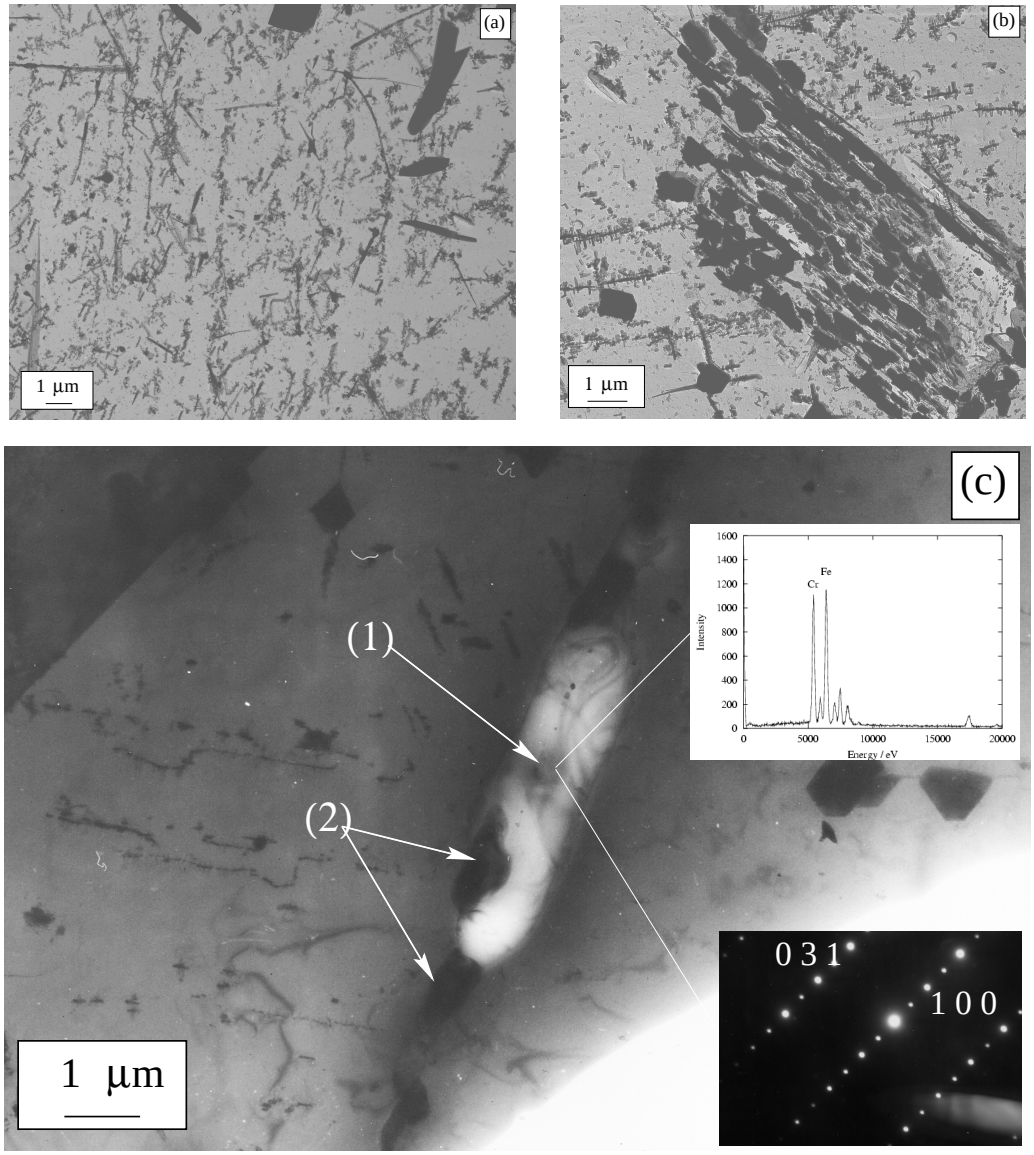

Figure 8.14: Carbon replicas of NF709R after 2500 h at 750 °C showing (a) the Z-phase precipitates as found after 200 h, and (b) coarse Cr_3Ni_2SiN and $M_{23}C_6$ precipitates on an incoherent twin boundary. (c) Thin foil of NF709R after 5000 h at 750 °C showing a large (c/1) σ-phase particle together with (c/2) Cr_3Ni_2SiN on a grain boundary.

8.7 Longer term ageing of NF709 and NF709R

All specimens were aged at least 10000 h at both temperatures, the longest ageing treatment reaching 17500 h at 750 °C for NF709R. Only results up to 10000 h are presented here.

Figure 8.15 shows optical micrographs of NF709 and NF709R after 10000 h at 750 °C and 800 °C. The precipitation is clearly denser in the specimen aged at 750 °C, with

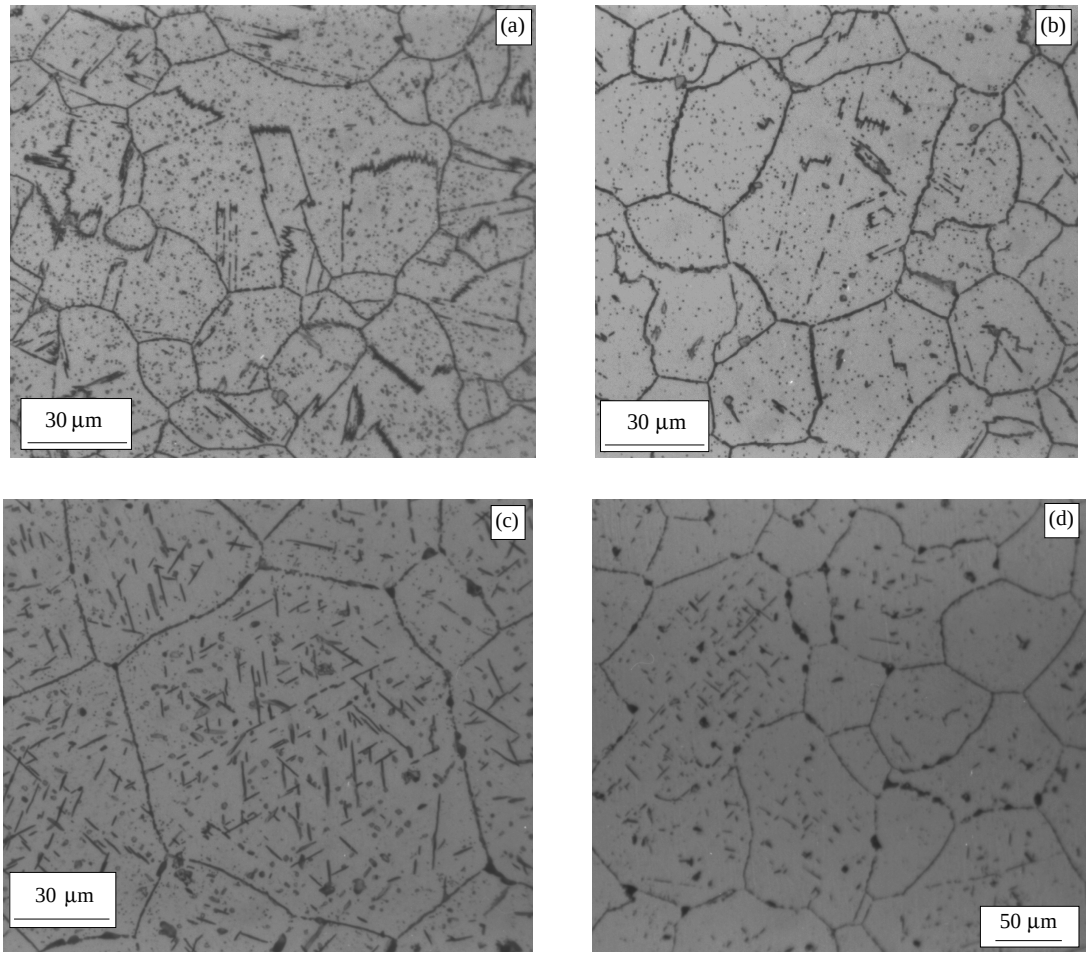

Figure 8.15: Optical micrographs of NF709 and NF709R aged 10000 h at 750 °C (a and c respectively) and 800°C (b and d respectively).

NF709 showing a stronger presence of $M_{23}C_6$ and Cr_3Ni_2SiN on twin boundaries and intragranularly (figure 8.15 (a) and (b)); NF709R shows a more even distribution of σ-

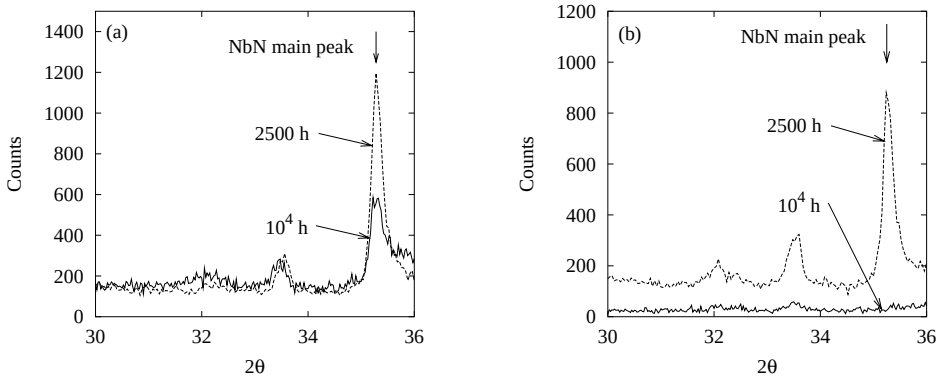

Figure 8.16: The main diffraction peak for NbN, (a) at 750 °C and (b) 800 °C for NF709 aged 2500 and 10000 h.

phase plates at 750 °C (figure 8.15 (c)). Following heat-treatment at 800 °C, σ-phase is present on grain boundaries and intragranularly (mainly in the larger grains) in NF709R.

The X-ray analysis of extracted residues revealed that, in NF709, NbN completely disappeared following heat-treatment at 800 °C and almost so at 750 °C (figure 8.16). This most likely follows the formation of CrNbN (Z-phase). As mentioned earlier, Z-phase, which is observed in transmission electron microscopy is not found using this method, probably because small CrNbN particles are dissolved during the extraction process. As for specimens aged 2500 and 5000 h, a separation is visible between $M_{23}C_6$ and Cr_3Ni_2SiN in the specimen aged at 800 °C but not for 750 °C; the lattice parameters were calculated to be:

Phase / Ageing time	5000 h	10000 h
$M_{23}C_6$	10.684 Å	10.679 Å
Cr_3Ni_2SiN	10.722 Å	10.712 Å

Table 8.8: The lattice parameters of $M_{23}C_6$ and Cr_3Ni_2SiN at 800 °C for two different ageing times.

Using TEM, it was possible to confirm the nature of the intragranular plates: figure 8.17(a) shows a thin foil of NF709R after 10000 h at 750 °C, in which large plates of σ-phase are found. The dislocations are decorated with Z-phase in a similar fashion as shown in previous figures. Large Cr_3Ni_2SiN particles were also found both on grain boundaries and intragranularly as illustrated in figure 8.17 (b) and (c).

Figure 8.18 shows precipitation on an incoherent twin boundary and on a grain boundary in NF709 after 10000 h at 750 °C. The particles have coarsened considerably when compared with similar observations after 100 h, as in figure 8.6 (b).

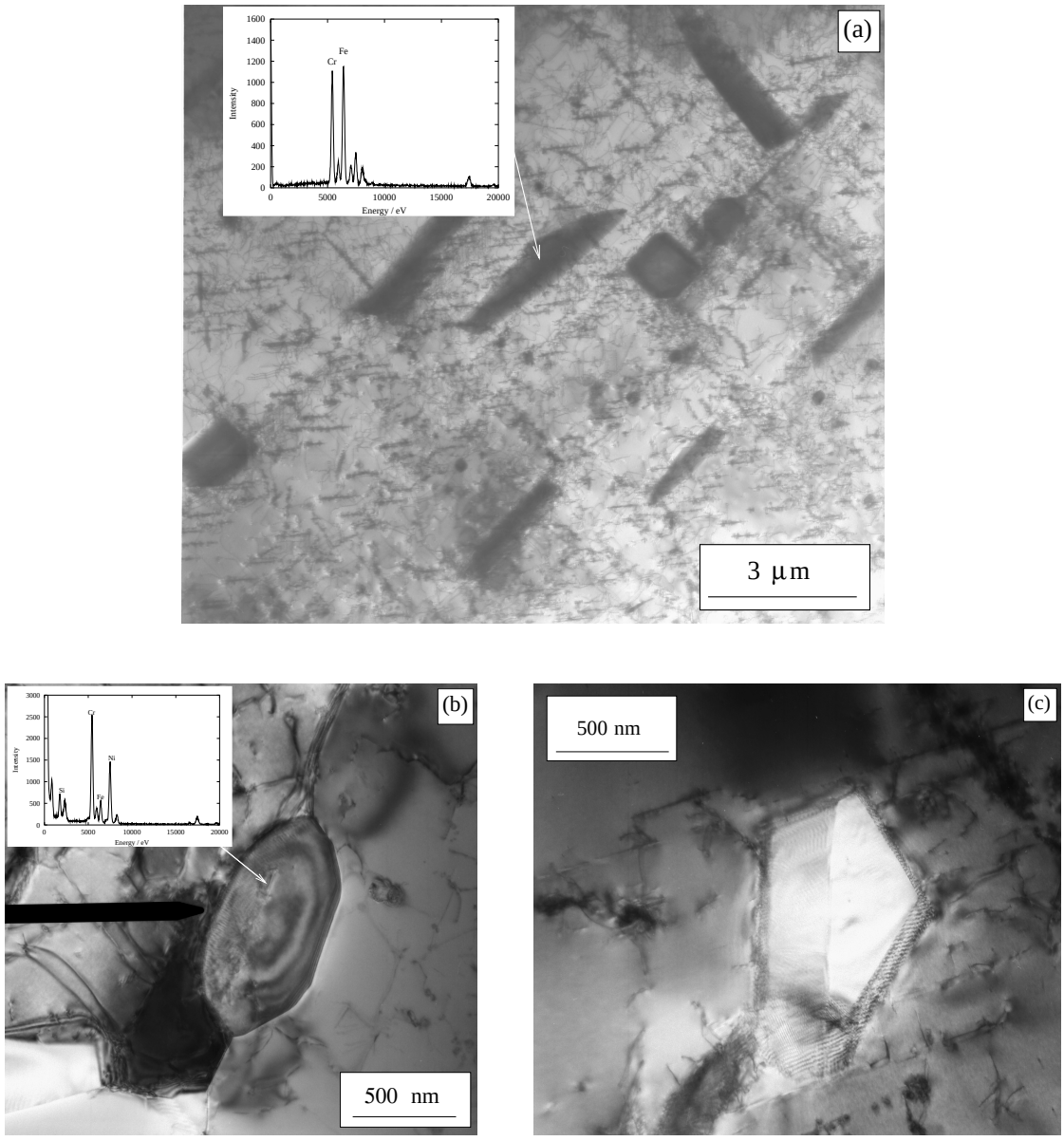

Figure 8.17: Transmission electron micrographs of a thin foil of NF709R aged 10000 h at 750 °C: (a) intragranular plates of σ phase and dislocations decorated by Z-phase. Cr_3Ni_2SiN (b) on grain boundary and (c) as an intragranular plate.

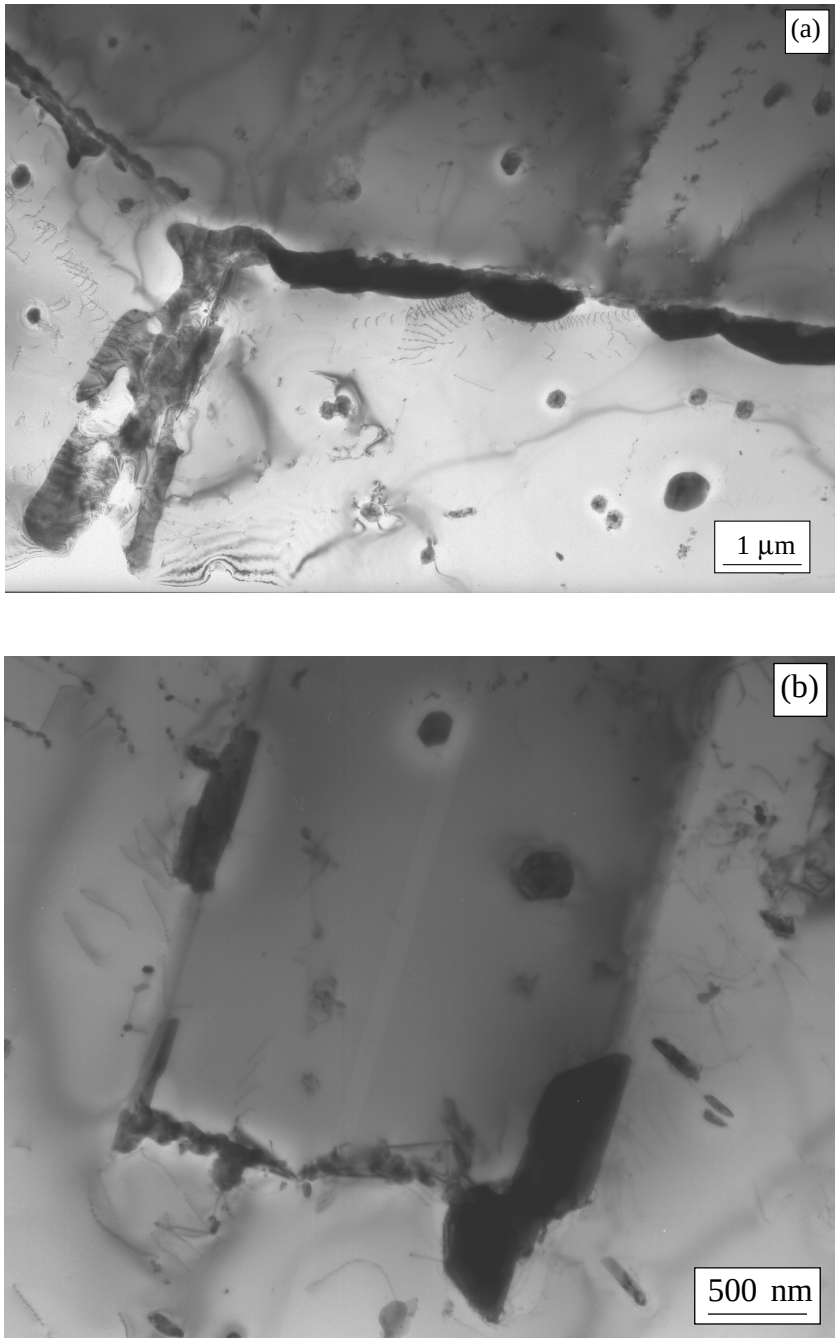

Figure 8.18: Transmission electron micrographs of a thin foil of NF709 after 10000 h at 750 °C, showing considerable coarsening of precipitates when compared to similar observations at shorter ageing times.

8.8 Summary and Discussion

8.8.a Summary

Table 8.9 summarises the phases observations at different times for NF709 and NF709R aged at 750 °C and 800 °C.

Time (h)	0	200	2500	5000	10000
NF709	NbN TiN (Nb,Ti)C	$M_{23}C_6$(+) Z-phase(+) NbN(-) TiN (Nb,Ti)C	$M_{23}C_6$(+) Cr_3Ni_2SiN(+) Z-phase(+) TiN NbN(-) (Nb,Ti)C	$M_{23}C_6$(+) Cr_3Ni_2SiN(+) Z-phase(+) TiN NbN(-) (Nb,Ti)C	$M_{23}C_6$(+) Cr_3Ni_2SiN(+) Z-phase(+) TiN NbN(-) (Nb,Ti)C
NF709R	TiN Z-phase	Z-phase(+) $M_{23}C_6$(+) TiN	Z-phase(+) $M_{23}C_6$(+) Cr_3Ni_2SiN(+) σ(+) TiN	Z-phase(+) $M_{23}C_6$(+) Cr_3Ni_2SiN(+) σ(+) TiN	Z-phase(+) $M_{23}C_6$(+) Cr_3Ni_2SiN(+) σ(+) TiN

Table 8.9: Summary of the different phases identified over the ageing treatments at 750 and 800 °C. (+) indicates a phase forming during the ageing treatment, (-) a phase dissolving. The same phases were identified at 800 °C although the quantities were, in some cases such as σ-phase, obviously different.

8.8.b Cr_3Ni_2SiN and G-phase in 20Cr/25Ni steels

Although M_6C is a quite frequently reported carbide in ferritic and austenitic steels containing Mo, as Fe_3Mo_3C, the structure sometimes referred to as η encompasses a much wider composition range [50] from $M_3M'_3X$ to $M_3M'_2SiX$, where M indicates a substitutional element such as Fe or Cr, while X indicates an interstitial element such as C or N. η is a diamond cubic structure whose lattice parameter varies in the range 10.6-12.4 Å.

Cr_3Ni_2SiX is a particular composition of the η structure, whose lattice parameter is 10.62 Å (JCPDS 17-330), which makes it extremely similar to $M_{23}C_6$ from a structural point of view, although the latter is cubic while the former is diamond-cubic. Very few studies report its presence under normal ageing conditions, while it is more frequently found in irradiated austenitic stainless steels.

In 1981, Titchmarsh and Williams [54] reported its presence in FV548, a Nb stabilised version of type 316 stainless steel. In this steel, Cr_3Ni_2SiC is not found under normal

In study	Cr	Ni	Mo	Mn	Si	Nb	C	N
Titchmarsh *et al.* [54]	16.5	12.0	1.44	1.14	0.35	0.92	0.11	-
Jargelius-Pettersson [55]	19.8	25.0	4.59	1.44	0.54	-	0.014	0.210
Powell *et al.* [60]	19.4	24.4	-	0.74	0.61	0.68	0.037	0.01

Table 8.10: Composition (wt%) of the steels investigated in some of the studies quoted.

ageing condition and its formation is attributed to the unusual segregation phenomena occurring in irradiated steels. In particular, point defect sinks are often surrounded by an increased amount of Si, because it is bound to the defects, and Ni, because it is slower than other elements to diffuse away from the sink. In both the works of Titchmarsh and Williams [54] and of Williams [53], the carbon content of Cr_3Ni_2SiC is assumed. This is supported by the fact that G-phase, another Ni, Si rich phase of composition close to $Ni_{16}Nb_6Si_7$ and space group Fm3m, forms instead of Cr_3Ni_2SiC in variants with a low level of carbon (0.02 wt%). A phase similar to Cr_3Ni_2SiC is reported by Jargelius-Peterson [55] in a 20/25 N-bearing steel, but as a nitride rather than a carbide.

The substitutional content of Cr_3Ni_2SiC undergoes significant changes as the temperature of ageing is modified. Williams [53] reports increasing amounts of Mo and Fe substituting for Cr and Ni respectively, when the ageing temperature increases. He therefore proposes the more general formula $(Cr, Mo)_3(Ni, Fe)_2SiC$. This study also gives evidence against the idea that Cr_3Ni_2SiC forms from $M_{23}C_6$ by infiltration of Ni and Si.

It is interesting to now study closely the precipitation of G-phase and η carbide under conventional ageing in 20/25 steels. The former phase is reported in various studies on 20/25-Nb stabilised steels [60, 65, 66], while report of the latter was only found for a 20/25 N-bearing steel, where it is rather a nitride than a carbide. Powell *et al.* [60, 65] and Ecob *et al.* [66] have found G-phase in a 20/25 Nb stabilised steel, and observed that NbC partially transforms to G-phase with time. Ecob *et al.* [66] have related the increasing relative instability of NbC compared to G-phase, in three different steels, to the amount of oxygen present in the steels. To justify this observation, they proposed that Si segregation was following oxygen segregation to the NbC particles, therefore creating the thermodynamic conditions required for the formation of G-phase. Nickel segregation may not be required in such steels, since the Ni content is more than double that of AISI 316 stainless steel.

On the basis of these observations, it is possible to argue that G-phase is more stable than Cr_3Ni_2SiC in these steels: segregation provides the increased Si level required, while the dissolution of NbC is expected to raise locally the carbon level. Both phenomena are expected to be favourable to the formation of Cr_3Ni_2SiC, which is nevertheless not observed.

It seems therefore reasonable to say that if either phase was to be found in NF709 or NF709R, it would be G-phase. However, none is observed, while Cr_3Ni_2SiN is present in significant quantities. In chapter 2, it has been proposed that observations on the effect of nitrogen on the formation of M_6C were better understood by considering M_6C and other compositions as occurrences of the same η structure. Again, the results here support the idea that the η structure is generally stabilised by nitrogen, whether its composition is Mo-rich or Ni/Si-rich.

8.8.c σ-phase formation and effect on mechanical properties

The difference between NF709 and NF709R is noticeable given the relatively small composition changes. As explained in chapter 2, σ-phase formation is favoured by both a high Cr and a low C content. The presence of σ-phase in NF709R but not in NF709 is therefore not surprising and is in fact predicted from the SGTE (Scientific Group Thermodata Europe) databases, using MT-DATA:

	NF709	**NF709R**
750 °C	0.8	5.9
800 °C	0	2.45

Table 8.11: The amount of σ-phase in wt%, predicted with MT-DATA for NF709 and NF709R, allowing for austenite, $M_{23}C_6$, M_6C, NbN, NbC, TiN, TiC, and σ-phase.

The role of σ-phase on mechanical properties, and particularly on creep strength, in austenitic stainless steels, is not clearly defined, and some attribute the main cause of a reduction of toughness to the general formation of carbides and nitrides [108].

The formation of copious amounts of σ-phase caused great concern about the ductility of NF709R after long term service. The results of creep tests provided by Nippon Steel were examined to identify the possible effects of the presence of this phase on the creep ductility. It is not clear what were the exact compositions of the steels used in the tests,

as only a label "22Cr" would distinguish some of the compositions tested. It was assumed that the "22Cr" labelled data were for NF709R while all others were for NF709.

As can be seen in figure 8.20, the results are the opposite of the expectations, with NF709R showing significantly better creep ductility, even for specimens with a rupture life of 5000 h and more, where σ-phase is expected in significant quantities.

An additional experiment was carried out to verify the deformation behaviour of the steels provided: after ageing 10000 h at 750 °C, samples of both NF709 and NF709R were deformed 30% in compression.

Figure 8.19 shows that grain boundary cracking was observed at various places in NF709, but nowhere in NF709R. Moreover, the micrographs show that the intragranular plates can deform to a limited extent.

These observations support the fact that carbide and nitride precipitation in general, rather than σ-phase alone, cause the embrittlement in these steels.

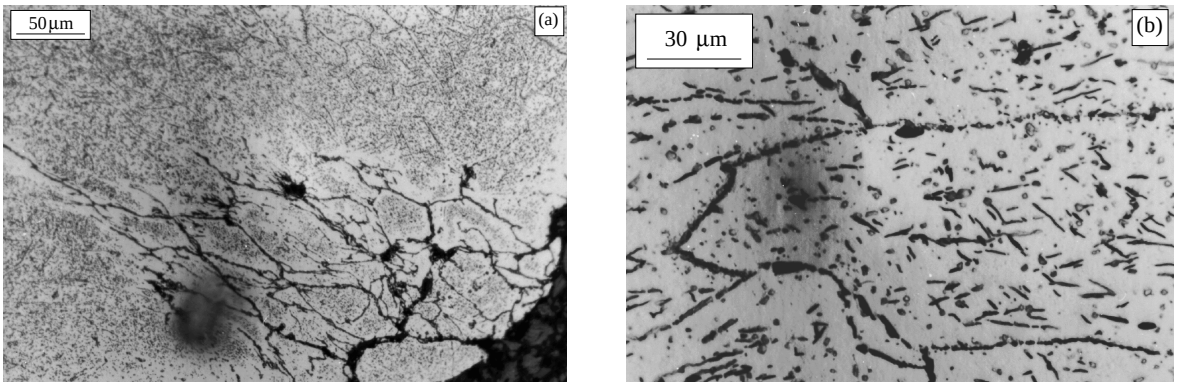

Figure 8.19: Optical micrographs of (a) NF709 and (b) NF709R deformed by 30% in compression after ageing 10000 h at 750 °C. Grain boundary cracking is observed at the corners of the specimen in NF709 (nowhere in the bulk material), not in NF709R. The intragranular plates of σ-phase are found to deform to a limited extent.

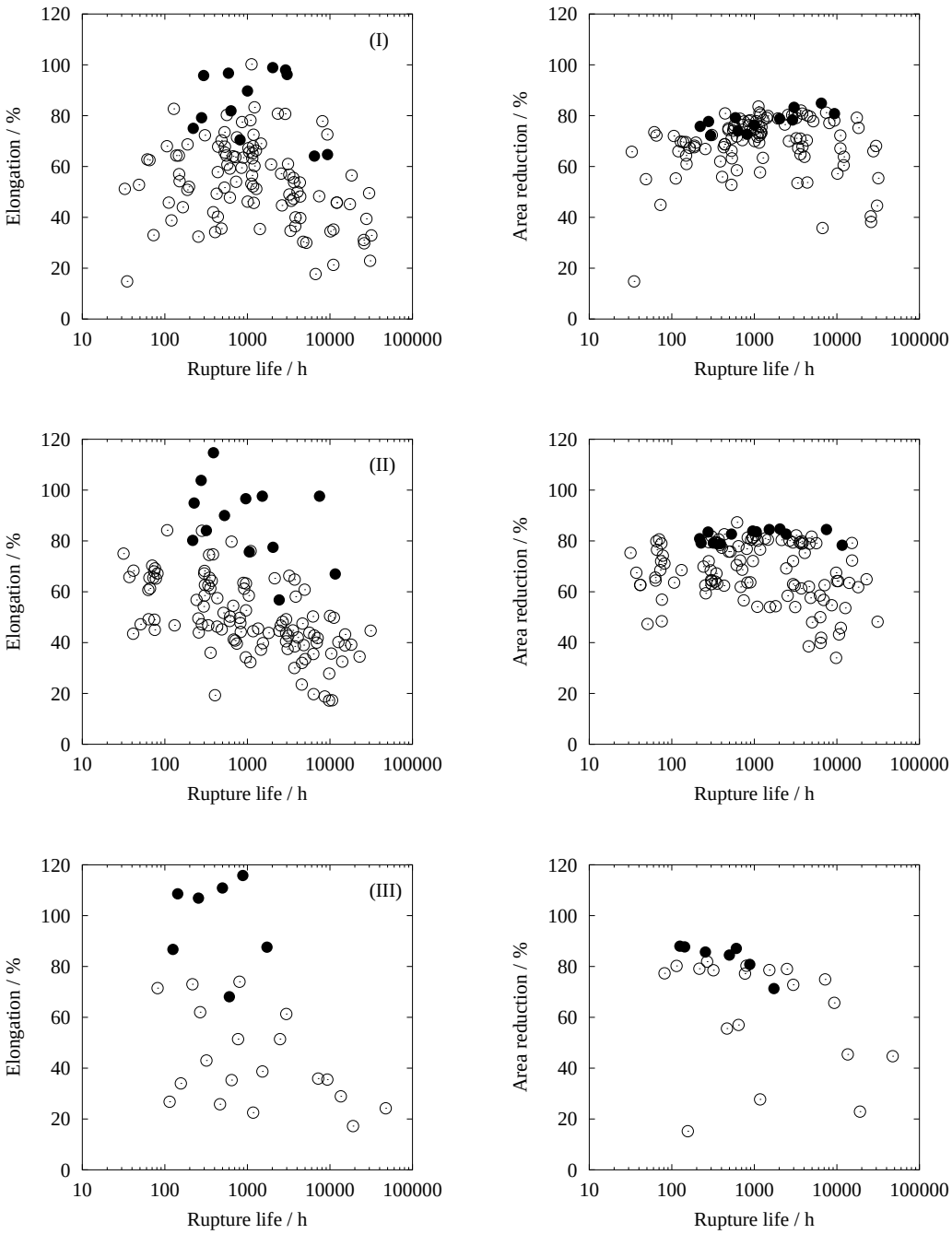

Figure 8.20: Creep elongation and reduction of area for the creep tests results provided by Nippon Steel at (I) 700 °C, (II) 750 °C, (III) 800 °C. ○ are for NF709, ● for NF709R.

8.8.d Quantifying the precipitation

The task of quantifying the amount of the different precipitates found in both NF709 and NF709R after different ageing times appeared impossible in practice. In the following, the different methods are presented with their limitations.

i Optical microscopy and scanning electron microscopy

For obvious reasons, most of the precipitates are not visible in optical microscopy. Small precipitates are not visible, while larger ones cannot be distinguished by morphology alone. Only σ-phase quantities could be estimated because of its particular appearance in scanning electron microscopy, when using backscattered electrons images (figure 8.21).

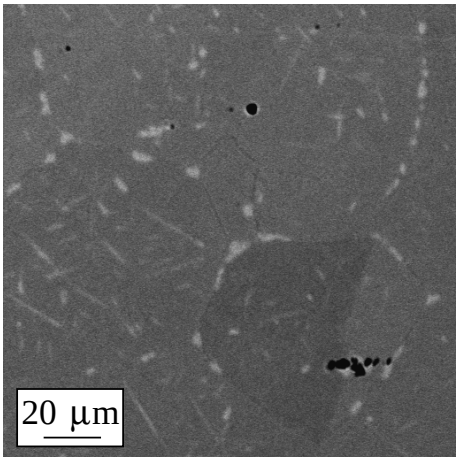

Figure 8.21: Backscattered electron image of grain boundary and intragranular σ-phase formed in NF709R after 10000 h at 750 °C, obtained in scanning electron microscopy. Because σ-phase does not contain interstitial elements such as C or N, it has, in average, a greater atomic number than the matrix and appears brighter. Carbides and nitrides, by contrast, are in average lighter than the matrix and appear darker, as can be seen on some grain boundaries.

ii X-ray analysis of extracted residues

The problem of quantifying the amount of the different phases present in a powder from its X-ray diffraction spectrum is well established. It is not possible to compare directly the areas of the peaks because different phases have different absorption coefficients which account for much of the intensity observed. In general, for a phase α in a polyphase specimen [109]:

$$I_{(hkl)\alpha} = \frac{K_e K_{(hkl)\alpha} X_\alpha}{\rho_\alpha \left(\mu/\rho\right)_s} \tag{8.1}$$

where $I_{(hkl)\alpha}$ is the intensity of the (hkl) diffracted line for phase α, K_e a constant for identical experimental settings, $K_{(hkl)\alpha}$ a constant for each diffraction line (hkl) of the phase α in the melange, ρ_α the density of the phase α, $(\mu/\rho)_s$ the mass attenuation coefficient of the polyphase specimen, and X_α the mass fraction of α in the melange.

Because the mass attenuation coefficient depends on the X_j:

$$\left(\frac{\mu}{\rho}\right)_s = \sum_j \left(\frac{\mu}{\rho}\right)_j \tag{8.2}$$

the problem is mathematically undetermined.

The conventional method to work around this difficulty consists of using a reference compound (corundum) added to the powder in a known quantity. With the help of calibration values providing the ratio of the intensity of a reference peak of the phase to quantify to that of corundum, it is possible to work out an amount present as a ratio of that of corundum. However, this requires that $I/I_{corundum}$ are known. This was only the case for $M_{23}C_6$ and σ-phase, but the peaks of the latter were for the most part hidden by peaks of other phases.

Further limitations of this method have been presented before concerning the size of the precipitates retained by the filter during filtration and the possible dissolution of the smallest particles.

iii Transmission electron microscopy

The smallest particles can only be seen during transmission electron microscopy, and in the case of Z-phase, only on carbon replicas. In TEM, phases such as $M_{23}C_6$ and Cr_3Ni_2SiN are difficult to distinguish on the basis of their morphology alone, and the use of EDX analysis is essential. This makes extremely time-consuming the identification of a number of particles large enough to provide reliable quantitative data, without mentioning the corrections required because TEM is in practice the observation of a projected volume.

A TEM based technique appears to be a promising method for reliable quantitative observations. Energy filtered TEM is similar to electron energy loss spectroscopy, but the whole image instead of a single beam is filtered according to the energy of the electrons. In this way, a composition map can be more or less easily obtained. However, the method is still under development and remains extremely time-consuming.

8.9 Conclusion

The precipitation sequence of NF709 and NF709R have been studied for heat-treatments of different duration at 750°C and 800°C. It has been shown that, despite their similar chemical compositions, these steels exhibit different precipitation behaviour. In particular, there is evidence that the nitride CrNbN, known as Z-phase, is more stable at higher temperatures in NF709R than in NF709. Also, σ-phase is found in copious quantities in the latter but not in the former.

With support of the existing literature, the formation of Cr_3Ni_2SiN in both NF709 and NF709R is taken as evidence that the η structure is generally stabilised by nitrogen.

To verify whether the formation of σ-phase was detrimental to the mechanical properties, the creep data provided by Nippon Steel were examined and aged specimens were deformed, with a unique conclusion that NF709R exhibits superior ductility when compared with NF709.

Different experimental techniques have been used together as it has been demonstrated that each presents serious limitations in a different domain of observation. In particular, evidence is given that small precipitates dissolve during the electrolytic dissolution of the austenite.